Article

Effect of Porosity on the Thermo-Mechanical Behavior of Friction-Stir-Welded Spark-Plasma-Sintered Aluminum Matrix Composites with Bimodal Micro- and Nano-Sized Reinforcing Al$_2$O$_3$ Particles

Behzad Sadeghi [1,*], **Behzad Sadeghian** [2], **Aboozar Taherizadeh** [2], **Aleksandra Laska** [3],
Pasquale Cavaliere [4,*] **and Arun Gopinathan** [5,6]

[1] Centre of Excellence for Advanced Materials Application, Slovak Academy of Sciences, 845 11 Bratislava, Slovakia
[2] Department of Materials Engineering, Isfahan University of Technology, Isfahan 8415683111, Iran
[3] Faculty of Mechanical Engineering and Ship Technology, Gdansk University of Technology, 80-233 Gdansk, Poland
[4] Department of Innovation Engineering, University of Salento, Via per Arnesano, 73100 Lecce, Italy
[5] Institute of Materials & Machine Mechanics, Slovak Academy of Sciences, 845 11 Bratislava, Slovakia
[6] Faculty of Materials Science and Technology, Slovenská Technická Univerzita, Ulica Jána Bottu č.25, 917 24 Trnava, Slovakia
* Correspondence: behzad.sadeghi@savba.sk (B.S.); pasquale.cavaliere@unisalento.it (P.C.)

Abstract: The thermo-mechanical behavior of nanosized Al$_2$O$_3$ particles reinforcing aluminum was analyzed in the present paper. The material was prepared by spark plasma sintering and friction stir welding. The thermal stresses affecting the composite behavior during welding were modeled through COMSOL MultiPhysics, and the results were validated by the analyses of the composites' mechanical properties. The spark-plasma-sintered materials presented limited porosity, which was taken into account during the modeling phase. Both model and experiments revealed that higher heat input is related to better material mixing during welding and sound mechanical properties. Thermal stresses lead to residual stresses close to 300 MPa in the thermo-mechanically affected zone for processing conditions of 1900 RPM and 37 mm/min. This leads to an increase in hardness up to 72 HV.

Keywords: spark plasma sintering; nanocomposites; friction stir welding; COMSOL; mechanical properties

1. Introduction

Spark plasma sintering (SPS) allows for the manufacturing of dense metal matrix composites starting from elemental metallic and ceramic powders [1,2]. The technique is capable of obtaining materials with very fine microstructures through reduced sintering times and relatively low temperatures [2–4]. Processing parameter tuning allows for a reduction in porosity and for an increase in the mechanical properties of the sintered materials [5,6]. In SPSed materials, porosity is believed to represent the major factor governing the composites' mechanical properties [7]. The precise tuning of SPS processing parameters also allows for the activation of various strengthening mechanisms in the sintered materials, especially in the presence of ceramic reinforcing phases [8,9]. For SPSed materials, friction stir welding (FSW) and friction stir processing (FSP) are demonstrated to improve the materials' mechanical properties due to the better ceramic particle mixing and distribution, as well as further grain refinement [10]. This aspect can be further optimized by employing controlled percentages of nanosized reinforcements inside the metallic phase [11,12]. Here, the control of processing parameters such as welding tool

rotation and welding speed is the fundamental aspect for the optimal grain refinement, leading to improved mechanical properties [13,14]. Grain refinement is improved again in the presence of nanosized ceramic particles [15]. In this general view, it is fundamental to model the friction stir welding process in order to define the effects of processing parameters on the thermo-mechanical behavior of the welded materials, which is directly related to the final mechanical properties. Thermal simulation along with residual stress prediction in the FSW process has been investigated in several papers [16–20]. However, the simulation of this process for porous parts, such as parts made by the SPS method, has not been studied. In the simulation of porous parts, the effect of porosity and immobile fluid should be considered in the equations to make the simulation results more realistic [21]. In this research, considering the heat transfer equations in porous media and simulating heat transfer and residual stresses in the structure in the form of multiphysics, the FSW process was modeled for aluminum-based materials produced by the SPS method. The aim of the present paper is to define the effect of processing parameters on the thermo-mechanical behavior of friction-stir-welded aluminum matrix composites produced via spark plasma sintering.

2. Experimental and Numerical Procedure

2.1. Model Description

In this study, the Finite Element Modeling (FEM) method was used to simulate the temperature distribution and residual thermal stresses. For this purpose, the Fourier heat transfer equation was used, considering porous media for three-dimensional geometry. This equation was applied by considering 3% porosity in the structure of the work piece, according to Equation (1) [21]. The effective material properties are presented according to Equations (2) and (3).

$$\left(\rho C_p\right)_{eff} \frac{\partial T}{\partial t} + k_{eff} \nabla^2 T = Q \tag{1}$$

$$\left(\rho C_p\right)_{eff} = \varnothing \left(\rho C_p\right)_S + (1 - \varnothing)\left(\rho C_p\right)_{IMF} \tag{2}$$

$$k_{eff} = \varnothing \, k_S + (1 - \varnothing) \, k_{IMF} \tag{3}$$

where ρ is the density, C_p is the heat capacity, k is the heat transfer coefficient and Q is the produced heat. Eff index means effective, S means solid phase and IMF means immobile fluid. $\varnothing$ is the solid volume fraction equal to 0.97. ρ, C_p and k for the solid phase, which is aluminum, are 2700 [kg/m^3], 24 [J/mol·K] and 210 [W/m·K], respectively. Moreover, for the immobile fluid phase, air, ρ, C_p and k, are 1.27 [kg/m^3], 29 [J/mol·K] and 0.025 [W/m·K], respectively. In order to consider the porosity in the model, the mixture law according to the first law of thermodynamics was used. According to Bejan's book [22], in order to model the energy equation for a homogeneous porous structure, the energy equation should be considered separately for each solid and immobile fluid phase. Then, the average of these equations should be considered for the whole system. In fact, in the software, the entire structure is considered as a bulk, and the material properties and volumetric averaging in the energy equations transform the structure into a porous medium.

The generated heat during the FSW process equation, which is the heat between the part and the tool, depends on the rotational speed, shoulder radius, coefficient of friction, coefficient of adhesion and slip. This equation was used according to Equation (4) [17].

$$Q = (\gamma \cdot f \cdot F(\omega r - u\psi Sin\theta) \tag{4}$$

where γ is a constant [17] and is equal to 1, ω is the tool rotational speed, r is the distance of each point under the tool from the tool center point, u is the welding velocity, ψ is a constant describing the effect of the affected side and retreated side and is equal to 20 [17,23], f is the ratio of the heat input to the work piece to the total heat, which is obtained according to Equation (5). ρ, C_p and k for the tool are 15E^3 [kg/m^3], 38 [J/mol·K] and 110 [W/m·K],

respectively. *F* is the parameter of generated heat due to friction and plastic deformation and is presented according to Equation (6).

$$f = \frac{\sqrt{(k\rho Cp)_\omega}}{\sqrt{(k\rho Cp)_\omega} + \sqrt{(k\rho Cp)_T}} \tag{5}$$

$$F = (1 - S)\tau\eta + S(\delta\tau\eta + (1 - \delta)\mu P_T) \tag{6}$$

where *S* is the slip parameter and also δ is the parameter related to adhesion. In fact, in the equation related to *F*, a distinction is made between friction heat due to pressure and the coefficient of friction, and heat due to plastic deformation, which depends on the shear yield stress of the material. In this equation, μ is the coefficient of friction equal to 0.4, P_T is the pressure due to the vertical force, τ is the maximum shear yield stress, and *S* is equal to 0.7. It is worth mentioning that the equations related to the calculation of *S* and μ have been mentioned in previous research [17,24,25].

The following equations show the different boundary conditions in this model. In these equations, the initial temperature of the work piece is equal to 300 K; the convection boundary condition with convection coefficient *h* = 10 (W/m²·K) for the upper surface according to Equation (7) and the sides of the part, and also h_b = 50 (W/m²·K), are considered for the lower surface of the part. Moreover, the boundary condition of heat transfer through radiation, according to Equation (8), was considered for the upper and side surfaces of the part, which includes the emissivity coefficient equal to 0.03 and Stephen Boltzmann coefficient equal to 5.67×10^{-8} [26,27].

$$k\frac{\partial T}{\partial n} = h(T - T_a) \tag{7}$$

$$k\frac{\partial T}{\partial n} = \varepsilon B\left(T^4 - T_0{}^4\right) \tag{8}$$

A thermo-mechanical model was used to predict the residual thermal stresses in the structure. Since no other strain is assumed in this model except thermal strain, the second part of the Equation (9) is applied. The thermal strain of this process was obtained from Equation (10) [20].

$$\varepsilon = \varepsilon^M + \varepsilon^T \tag{9}$$

$$\varepsilon^T = \alpha\Delta T \tag{10}$$

In the above equation, ε^M is the strain caused by mechanical work, ε^T is the thermal stress and α is the coefficient of thermal expansion of aluminum equal to 23×10^{-6} (1/°C). All the boundary conditions are schematically shown in Figure 1.

In this model, two sheets were considered side by side. The dimensions of each sheet were considered to be $150 \times 60 \times 3$ mm³ and tetrahedral elements were applied for meshing; these elements were employed because of the most affordable results obtained in previous training simulations. It should be noted that the tool geometry was assumed according to Figure 2. All stages of model construction, meshing and solving were accomplished by COMSOL Multiphysics version 5.3 software (COMSOL AB, Stockholm, Sweden).
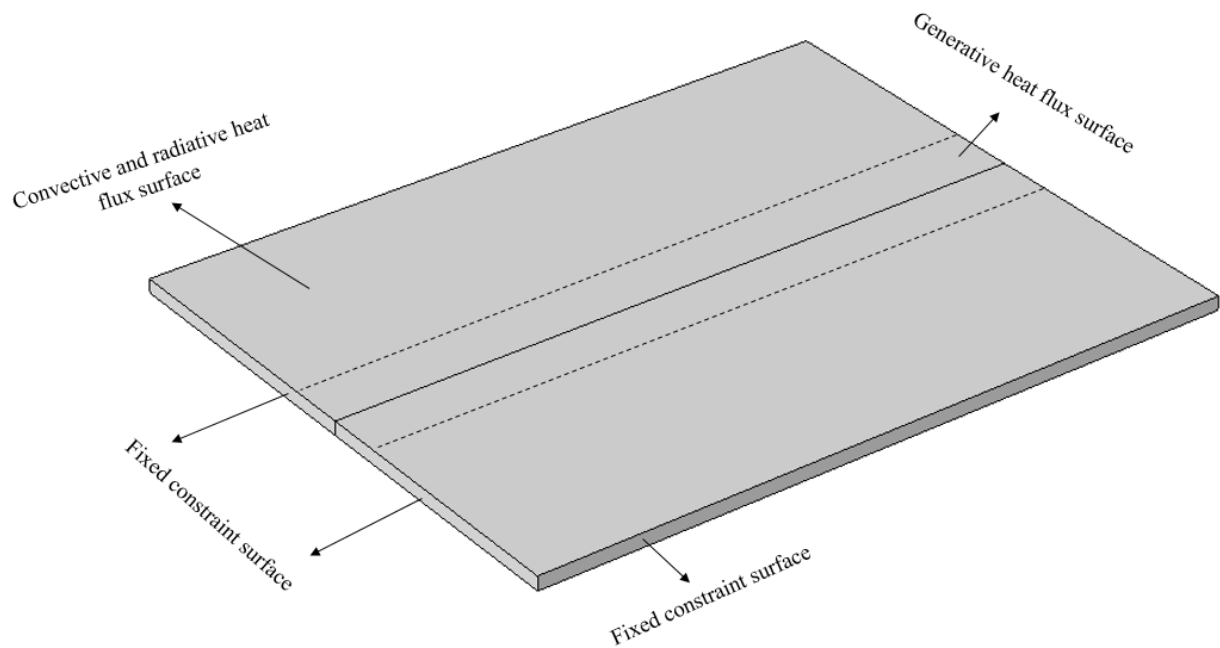
Figure 1. Schematic illustration of the boundary conditions used in thermal and mechanical simulations.
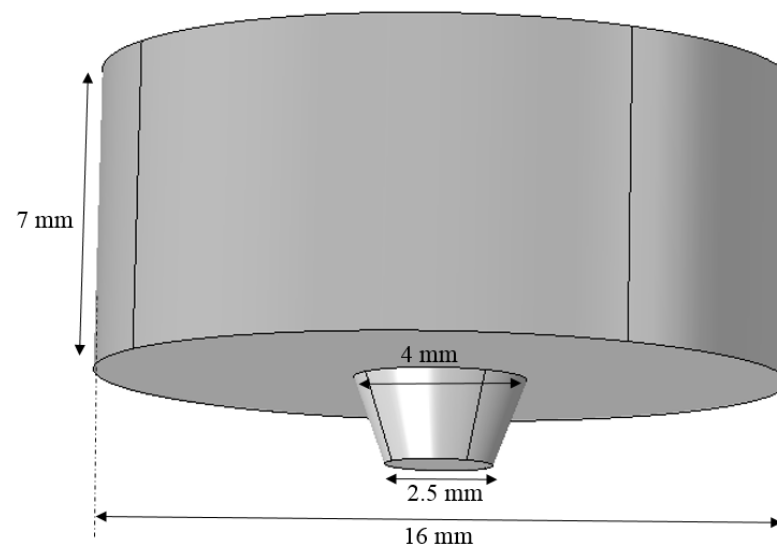
**Figure 2.** Schematic illustration of tool geometry used in the simulations.

2.2. Material Preparation and Characterization

Disks of pure aluminum reinforced with 10% of Al_2O_3 particles were produced via spark plasma sintering. The ceramic phase percentages were 8% in volume of Al_2O_3 nanoparticles with mean dimensions of 40 nm (Evonik Industries, Essen, Germany) and 2% in volume of Al_2O_3 microparticles with mean dimensions of 15 μm (Sigma Aldrich, St. Luis, MI, USA). The spark plasma sintering procedure is detailed in [1]. Cylindrical samples with 40 mm in diameter and 5 mm in thickness were produced. Then, they were cut and friction-stir-welded. The employed tool geometry was described in [1,28]; it had a conical-shaped tool. The employed tilt angle was 3°. The welds were produced on a milling machine (Ferrari, Modena, Italy). The employed welding/processing parameters were 1900 RPM and 37 mm/min and 1600 RPM and 32 mm/min in order to fix the revolutionary pitch close to 50. These processing parameters were chosen because of previous results regarding the soundness of the welds [1]. The material's microstructure was characterized

through optical and scanning electron microscopy (SEM, Zeiss EVO 40, Zeiss, Oberkochen. Germany). In addition, the fracture surfaces of the tested materials were observed through SEM. The mechanical properties of the friction-stir-welded materials were characterized through microhardness measurements. Microhardness was measured at the center of the cross-section of the joints through a Vickers microhardness tester (Future-Tech FM-800, Tokyo, Japan) with the load of 2 N and the dwell of 10 s for each indent. Tensile tests were performed on specimens cut through electro discharge machining with the center of the cross-section corresponding to the center of the weld line. The gauge length of the tensile test specimens was 25 mm; the square cross-section was 5×5 mm^2. The tensile tests were performed with a Zwick/Roell standard testing machine (Zwick/Roell, Genova, Italy) with a constant strain rate of 1×10^{-4} s^{-1}.

3. Results and Discussion

The microstructure of the composite at different magnifications after spark plasma sintering is shown in Figure 3. When the SPS process is conducted, the developed electric potential of the aluminum particles due to the presence of non-conductive ceramic particles can crack the oxide layer. It develops the direct contact between metal particles with very low porosity, close to 3% [14], which is less than the porosity value reported in [29]. Such low porosity confirms the better bonding both in Al-Al bonding and Al-nano-sized Al$_2$O$_3$ at the grain boundaries of Al grains. It can be due to the fact that the atomic diffusivity of the nanoparticles is higher than that of the micron-sized particles. In addition, the essence of the SPS technique as pressure-assisted sintering, as well as the rendering of clean grain boundaries as a consequence of the formation of plasma between existing spaces between aluminum grains during the SPS process, is another fact that can explain the formation of a strongly bonded microstructure in the Al-Al$_2$O$_3$ composite. In contrast, the micron-sized Al$_2$O$_3$ particles, with lower atomic diffusivity compared to nano-sized ones, create extra space to become accommodated into the aluminum matrix. Indeed, the nano-sized Al$_2$O$_3$ particle size is much smaller than the matrix particle size, and hence the inter-particle voids created by the consolidation of aluminum particles have been occupied by the Al$_2$O$_3$ nanoparticles, leading to such a low-porosity sintered composite. Some dark and angled Al$_2$O$_3$ particles, mostly with micron size, are observed along the grain boundaries and triple points of aluminum grains, which explains the uniform dispersion of the reinforcement in the aluminum matrix. In addition, the appearance of aluminum grains in the microstructure shown in Figure 3a leads to a relatively heavily deformed structure, which is in line with the results reported in [30].
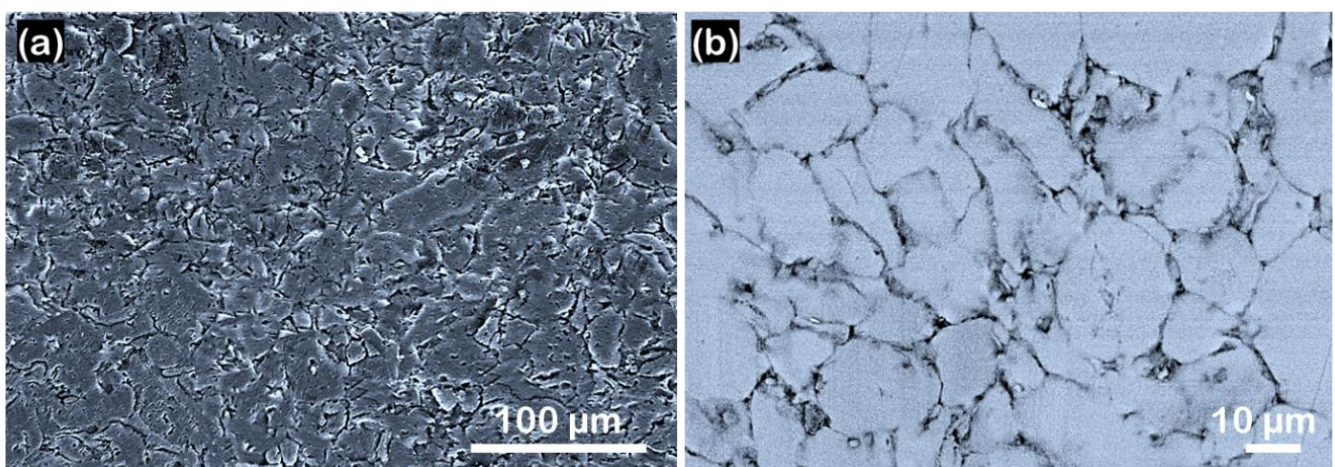
**Figure 3.** Microstructure of the studied composite after spark plasma sintering at different magnifications. (**a**) 100 μm; (**b**) 10 μm.

The incipient fusion phenomenon occurred to a vast extent between aluminum grains, even in the presence of Al_2O_3 dispersoids. It is probably due to the formation of plasma at inter-particle contacts at the time of sintering. However, the poor bonding of aluminum and Al_2O_3 nanoparticles has been reported in the literature in conventional sintering [31]. The Al_2O_3 particles in the range of nano to micron size are depicted with a more highly magnified SEM image of the sintered specimen in Figure 4. The agglomerates of Al_2O_3 with large content of nanoparticles are visible as the lighter area in the SEM image. Its presence is visible in the metal grain boundaries. The microscopic Al_2O_3 particles appear uniformly distributed. Otherwise, the nanometric particles are distributed along the grain boundaries and inside the grains. It seems that the agglomeration of Al_2O_3 particles is dependent on the size of Al_2O_3 particles, as most of the Al_2O_3 agglomerates are composed of nano-sized Al_2O_3 particles. In addition, higher agglomeration leads to higher porosity [14,32,33]. There is no significant grain growth after the SPS process. This is attributed to the SPS technique, which typically provides higher density under low-temperature conditions [2,3,34]. However, wherever the micron-sized Al_2O_3 particles settled, a few aluminum grains depicted some grain growth, which probably could be attributed to the inability of the micron-sized Al_2O_3 particles to pin down the grain growth at a larger scale.
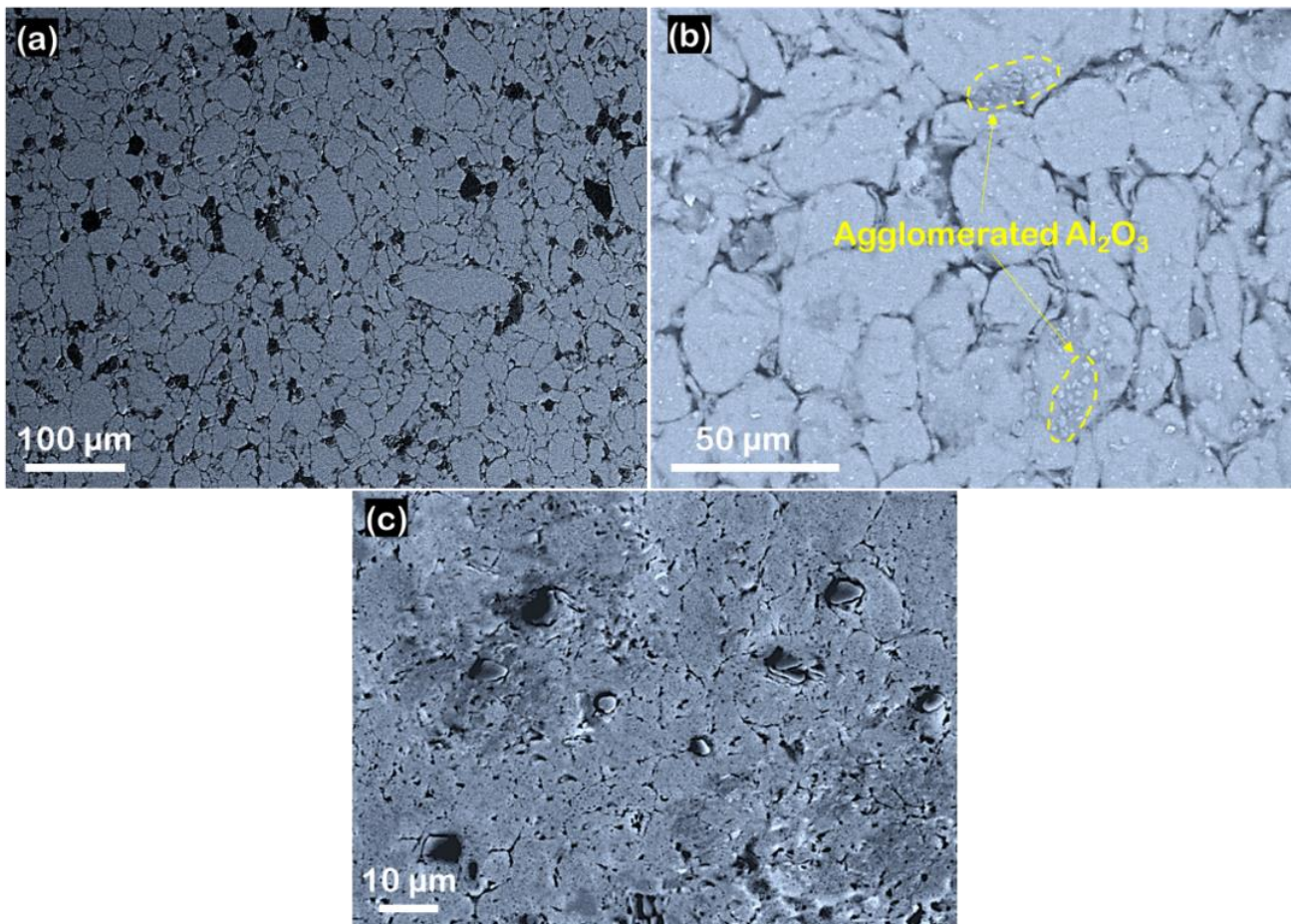
Figure 4. SEM microstructure of the composite after SPS (**a**) showing the distribution of microscopic and agglomerated nanoscopic Al_2O_3 particles, (**b**) clustering of nanoparticles at particle necks and inside the different grains (marked by yellow dashed line) and (**c**) larger alumina particles.

The distribution is revealed by the X-ray maps shown in Figure 5. The Al_2O_3 nanoparticles are present in the interspaces of aluminum particles (Figure 5a). The occurrence of nanoparticles greatly increases the work hardening rate of the Al matrix. Indeed, as Figure 5c1–4 show, individual nano-sized Al_2O_3 particles (mostly in the aluminum grain

interior) and individual micron-sized Al_2O_3 particles (mostly at the aluminum grain boundaries) effectively act to hinder the recovery and recrystallization processes of the Al matrix via the Zener drag effect [35,36] and keep the dislocations produced in heavily deformed aluminum grains in the microstructure, thus increasing the strain hardening capacity. In addition, the presence of hard and non-deformable tiny particles in a ductile matrix enhances the grain refining process. In addition, it is confirmed that nano-sized Al_2O_3 particles have a more effective role in grain refinement compared to micro-sized Al_2O_3 particles [14,32,37,38]. In this regard, the nano-sized Al_2O_3 particles hinder grain boundary migration, which restricts the grain growth. The smaller the grain size, the larger the grain boundary area, enhancing the effective obstacles as well as increasing the probability of Al_2O_3–dislocation interaction in the sintered microstructure. Obstruction of the dislocation motion hinders the onset of plasticity, which eventually results in improved tensile strength.
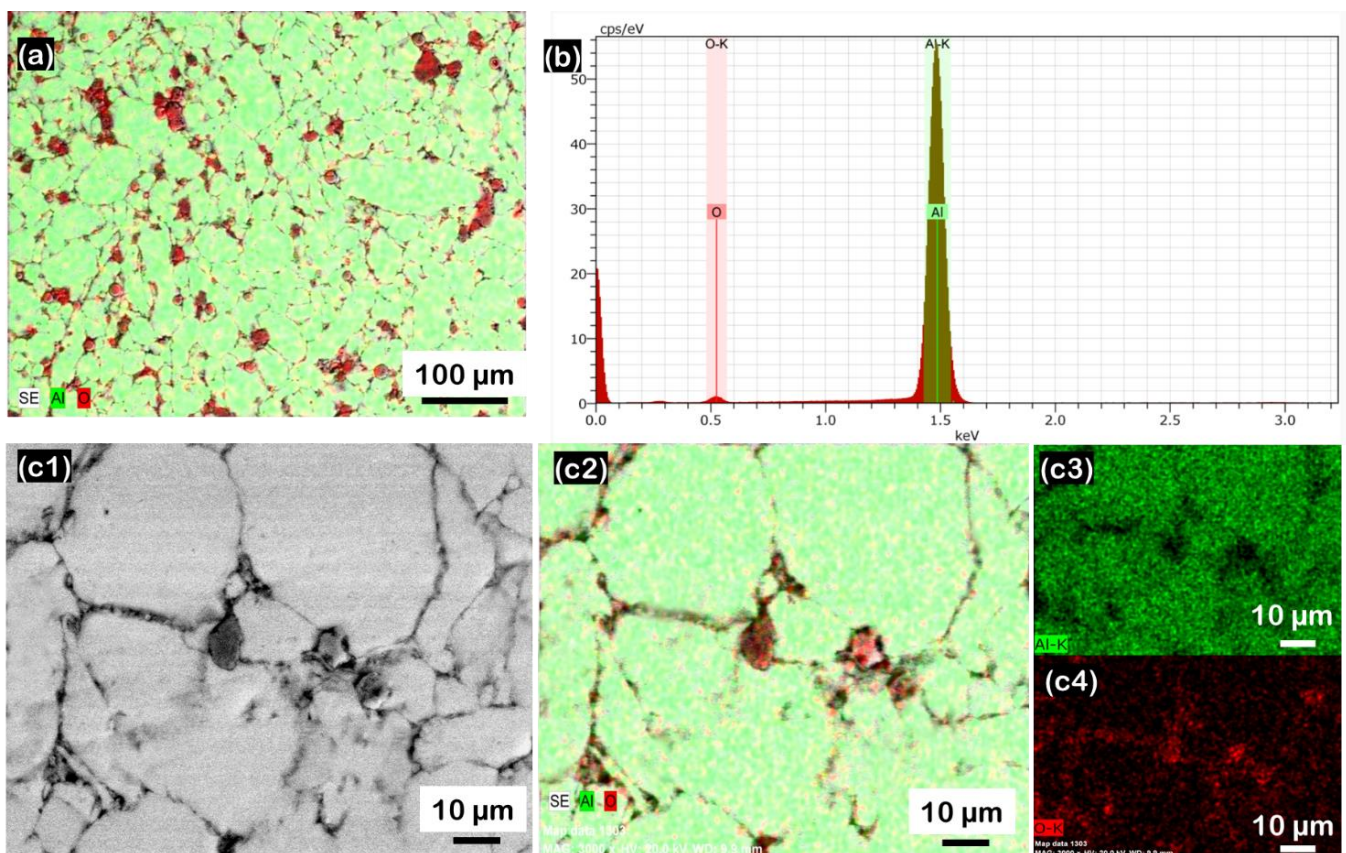

Figure 5. EDS analysis of SPSed Al/Al_2O_3 composite: (**a**) EDS map, (**b**) EDS spectrum of the analyses of the SEM images shown in Figure 2a, (**c1**) SEM, (**c2**) EDS map and (**c3**,**c4**) the corresponding analyses of the aluminum and oxygen elements, respectively.

From the X-ray map, it is evident that the presence of aluminum and aluminum oxide is detected in the sample. Aluminum carbide is absent in the sample, which is shown in Figure 5b. The X-ray map shows the larger Al peak with smaller Al_2O_3. Our previous results showed that with increasing Al_2O_3 nanoparticle content, the peak broadening increases while the crystallite size of Al decreases [1,32,39]. In addition, it also reported that the rise of nanoparticles leads to the hard agglomerates' development. Further, it hinders the local plastic deformation of Al particles. This leads to the formation of stains of Al_2O_3 nanoparticles in the Al matrix.

The simulation results of temperature distribution according to Figures 6 and 7 were obtained for welding parameters 1600 and 1900 rpm, respectively.
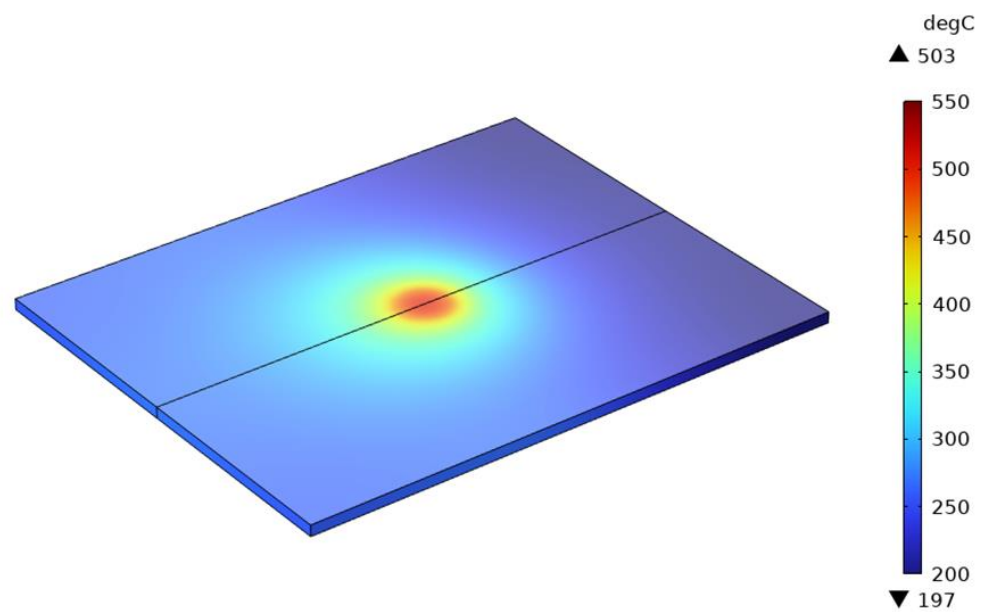
Figure 6. Three-dimensional plot of simulated temperature distribution in FSW of spark-plasma-sintered aluminum with 1600 RPM rotational speed.
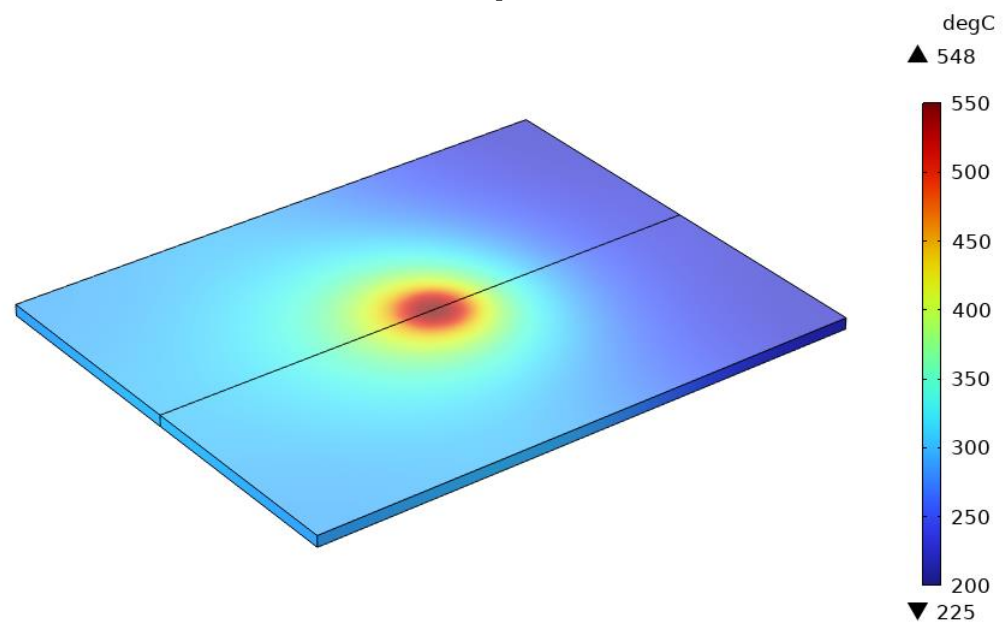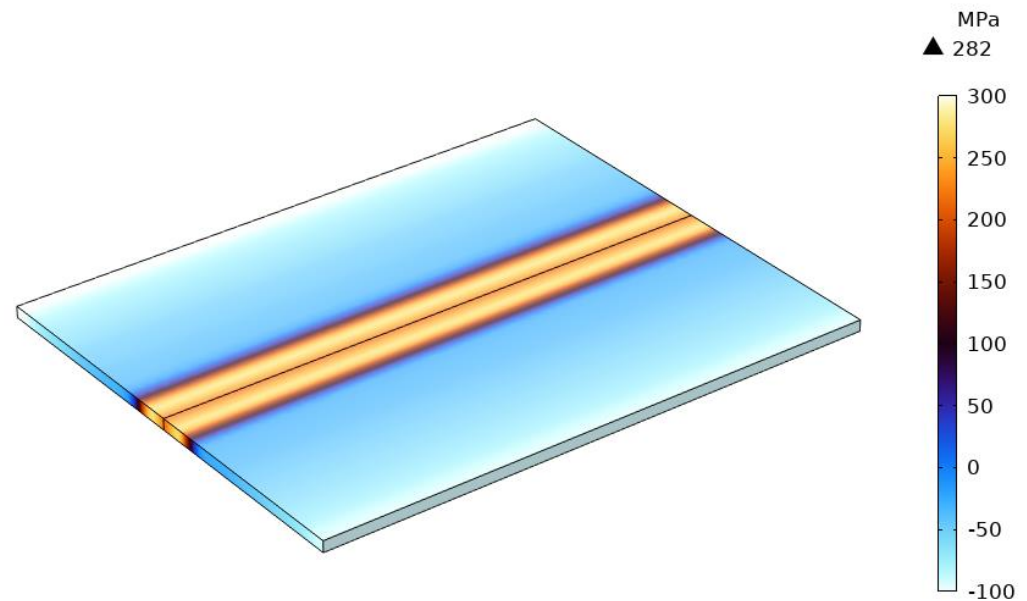
Figure 7. Three-dimensional plot of simulated temperature distribution in FSW of spark-plasma-sintered aluminum with 1900 RPM rotational speed.

Considering the general pattern of the three-dimensional contour of the temperature distribution in the plates, it is observed that this pattern is in proper agreement with the experimental results obtained from previous studies [40]. Therefore, FEM is an appropriate tool to simulate this process.

It is observed that increasing the rotational speed increases the maximum temperature in the parts during welding. In fact, increasing the rotational speed from 1600 rpm to 1900 rpm resulted in a 9% increase in the maximum temperature in the parts. Moreover, by increasing the rotational speed, we increase the heat generated due to the application of more friction cycles per unit time to the work piece. In addition, increasing the rotational speed increases the strain rate, which results in more shear strains per unit time [23,41]. Therefore, due to the increase in the *F* parameter (according to Equation (6)), there is an increase in the generated heat during FSW in the piece. Comparing the results of the

thermal simulation of the present study on the structure with a porosity of 3% with the results of previous research, it is observed that the simulated temperature value in the weld line in a plate with 3% porosity has a higher value than the average temperature of simulations on bulk aluminum [18,20,42].

Figures 8 and 9 show the results of the distribution of residual thermal stresses in the components during the FSW process. The temperature distribution is used as the primary input to calculate the residual stress distribution. In fact, the pattern and history of temperature distribution has a significant effect on the distribution of residual stress in the parts.

Figure 8. Three-dimensional plot of simulated residual thermal stress distribution in FSW of spark-plasma-sintered aluminum with 1600 RPM rotational speed.
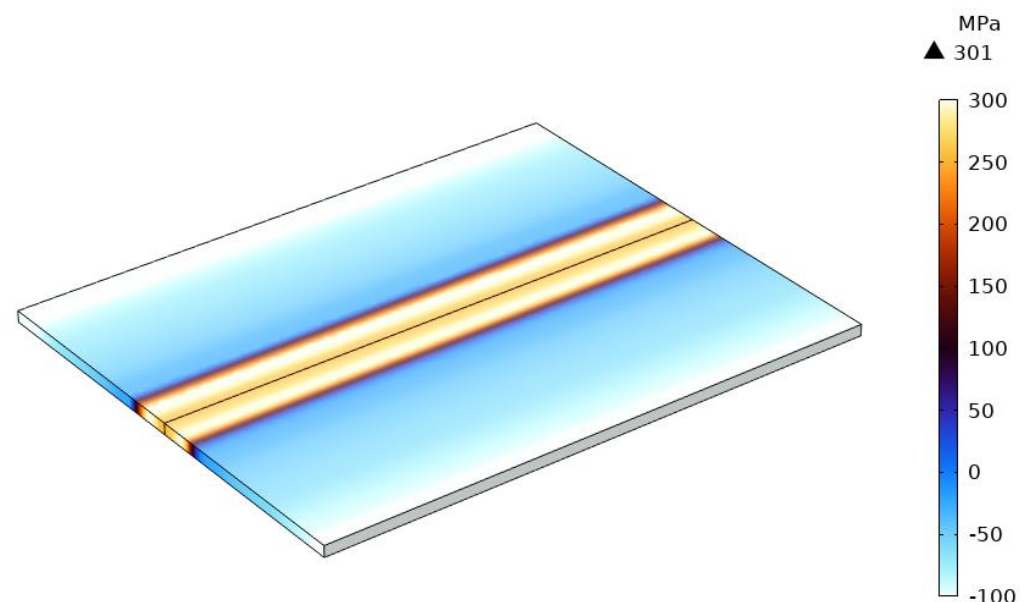
**Figure 9.** Three-dimensional plot of simulated residual thermal stress distribution in FSW of spark-plasma-sintered aluminum with 1900 RPM rotational speed.

The general diagram of the residual stress distribution is in good agreement with the results of previous studies [18,19]. After generating the heat input with the tool during the FSW process, the temperature rises in the welding center line and decreases after the

tool passes through. This causes residual thermal stresses in the structure. As can be seen, the residual thermal stresses are a combination of tensile and compressive stresses. The residual thermal stress in the FSW process is due to the expansion and contraction of the material during heating and cooling, when the sheets are fixed. It is observed that the 1900 rpm sample has a higher longitudinal stress. This is due to the higher maximum temperature in the components during this process, which results in more residual thermal stress in the structure. Figure 10 shows a diagram of the longitudinal stress changes in the cross-section of the parts. Comparing the results of temperature and stress distribution during the FSW process [20], it was observed that increasing the temperature increases the residual stress in the structure. This is also consistent with the results of the present study.
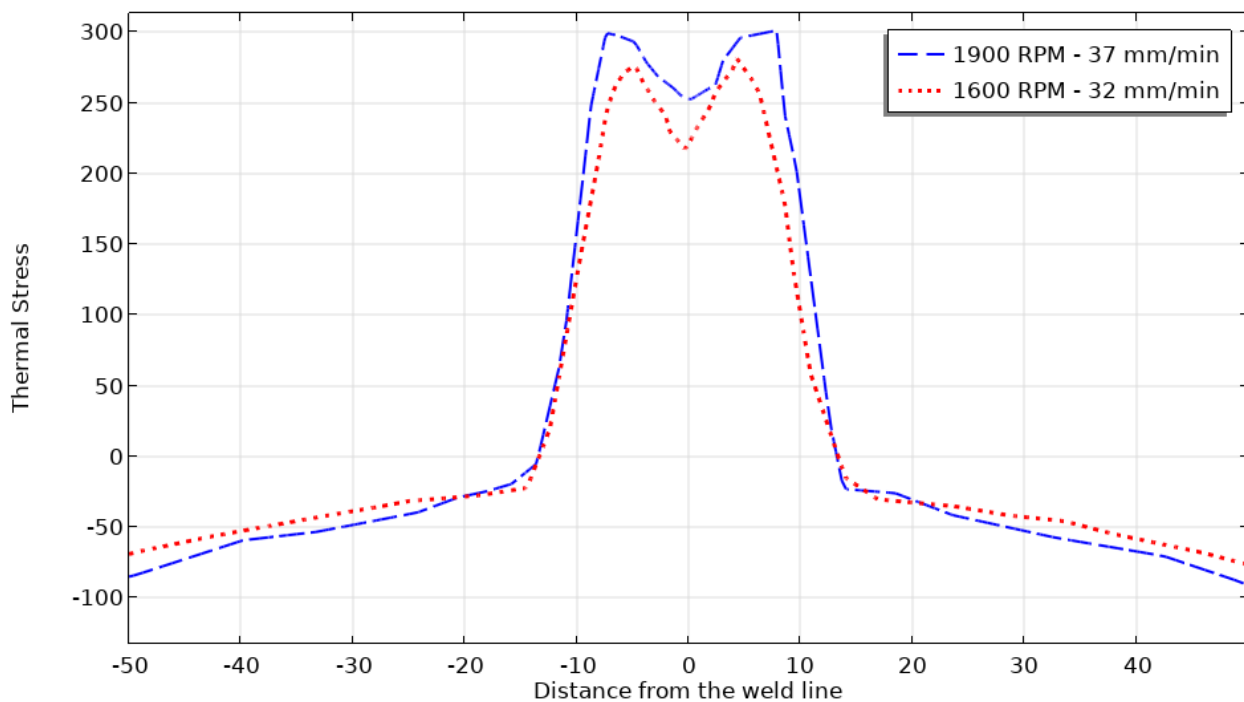
Figure 10. Longitudinal stress profiles for different welding parameters.

It is observed that from the center line to the side walls of the parts, the stress changes are accompanied by a steep slope, and then these changes have a gentle slope and the compressive stress on the sides can be observed. This is due to the steep temperature gradient from the center to the sides during the process. Moreover, as can be seen in the welding center, the residual stresses are weaker than those at the edges of the weld zone, due to the lower temperature in the center weld line compared to the edges of the weld zone. In fact, the heat generated depends on the radius of the tool shoulder. Therefore, the temperature is higher in areas that are as far away from the center line as the tool shoulder radius, resulting in higher thermal stress. The presence of porosity in the aluminum reduces the thermal diffusivity coefficient in the part [29]. Therefore, the temperature is distributed at a lower rate than in the bulk state structure. As a result, the temperature in the center line of the parts is higher than in the bulk state, and, therefore, after cooling, the residual thermal stress in the center line of the section will be higher. In fact, increasing the porosity causes greater temperature concentration in the center line of the part, which leads to an increase in residual thermal stress in the middle of the part due to greater thermal expansion. Observing the results of Poolperm et al.'s [43,44] research, it is confirmed that the presence of porosity increases the residual stress in the structure during the welding process. This has been validated in their research by measuring the residual stresses by the X-ray diffraction (XRD) method and also using FEM simulation and is in good agreement with the present study.

The samples were friction-stir-welded to pure aluminum sheets and the aspect for selected conditions is shown in Figure 11. Top views of all the welded/processed surfaces appear without the presence of defects, large voids and cracks, as previously reported by [1,2]. However, at lower ratios of rotating speed to travel speed (lower heat input), some surface inhomogeneities appeared (their images are not given), while, with a higher input of heat caused by the higher ratio of the rotating speed to the travel speed, the appearance of the welded zone is much better, without any type of defect. The investigation of the forces acting on the tool is crucial to understanding the nature of the material at the processing time.
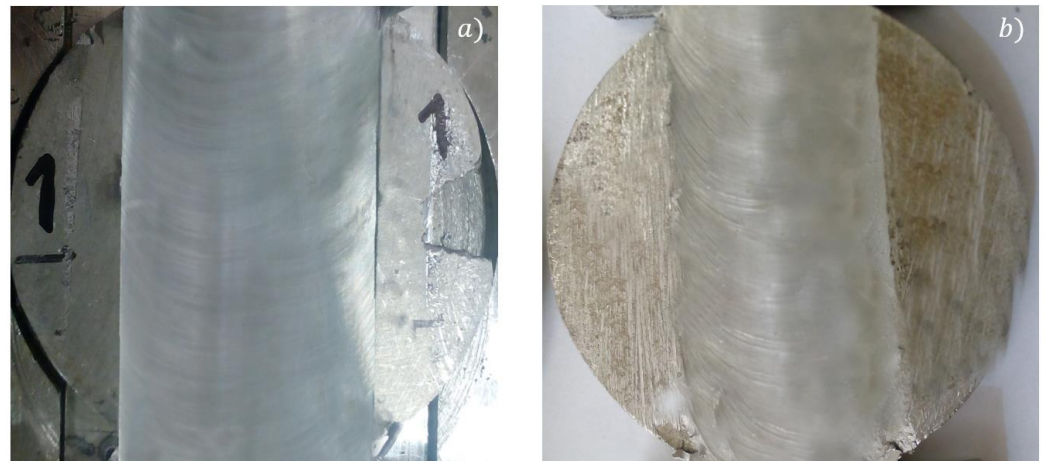
Figure 11. Aspect of FSWed samples after joining at different processing parameters, showing the surface aspect of the welds: 1900 RPM-37 mm/min (**a**), 1600 RPM-32 mm/min (**b**).

In general, the heat generation is determined by the coefficient of friction, speed of rotation and movement and moving direction. In particular, the rotation and moving speed raise the heat input [28,45,46].

It is well known that microstructural evolution during FSW is due to the heat input provided during processing. Heat input (*HI*) was calculated through Equation (11).

$$HI = \frac{2\pi}{3} \cdot \mu \cdot P \cdot W \cdot V \cdot R \tag{11}$$

μ is the local coefficient of friction; W and V are the rotation and travelling speeds, respectively; P is the axial force; R is the shoulder radius.

The force acting on the tool and the corresponding heat input in the welded sheets are described in Figure 12.

With an increase in the traveling speed, the force in the z-direction (Fz) increases. The tool–material friction and the severe plastic deformation during processing lead to a temperature variation within the range of 0.6–0.9 in the material melting temperature in the friction-stirred materials. In agreement with [1,28], the Fz is dependent on the processing parameter, so, as the Fz increases, the heat input increases. It exerts not only an influence on grain refinement, the grain size distribution between the nugget zone, thermo-mechanically affected zone and heat-affected zone and the dislocation density, but also leads to variation in the mechanical properties [1,28,45]. Indeed, there is no possibility to perform FSW on a bimodal-sized Al_2O_3-reinforced aluminum matrix nanocomposite if the heat input value is lower and higher than 28,000 and 57,000 J/mm, respectively [1,14]. The friction of the tool against the material, in addition to the non-elastic deformation, raises the temperature in the friction-stirred material. The temperature difference of 0.6–0.9 is developed by the movement and rotating speed of the tool, which melts the material [47].
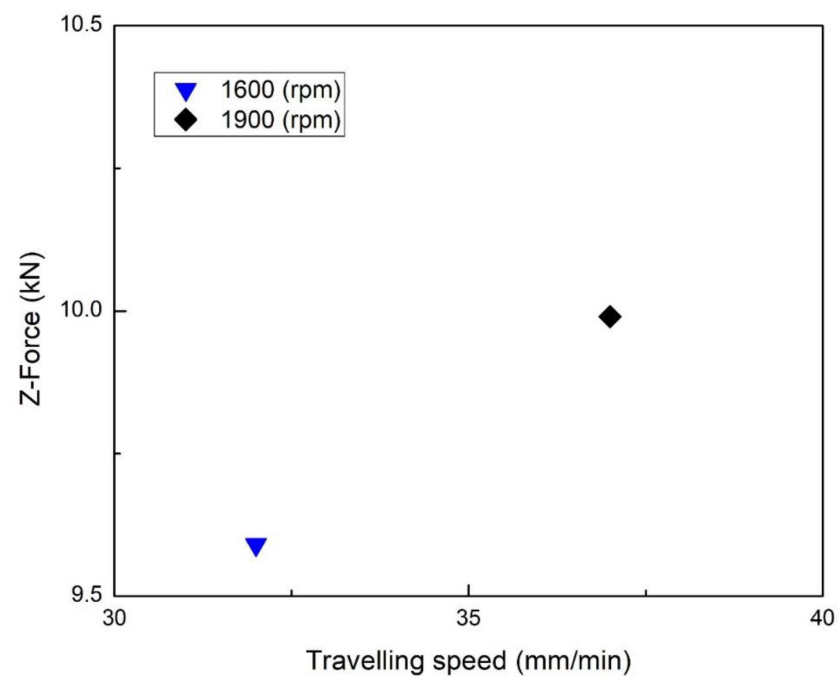
(**a**)
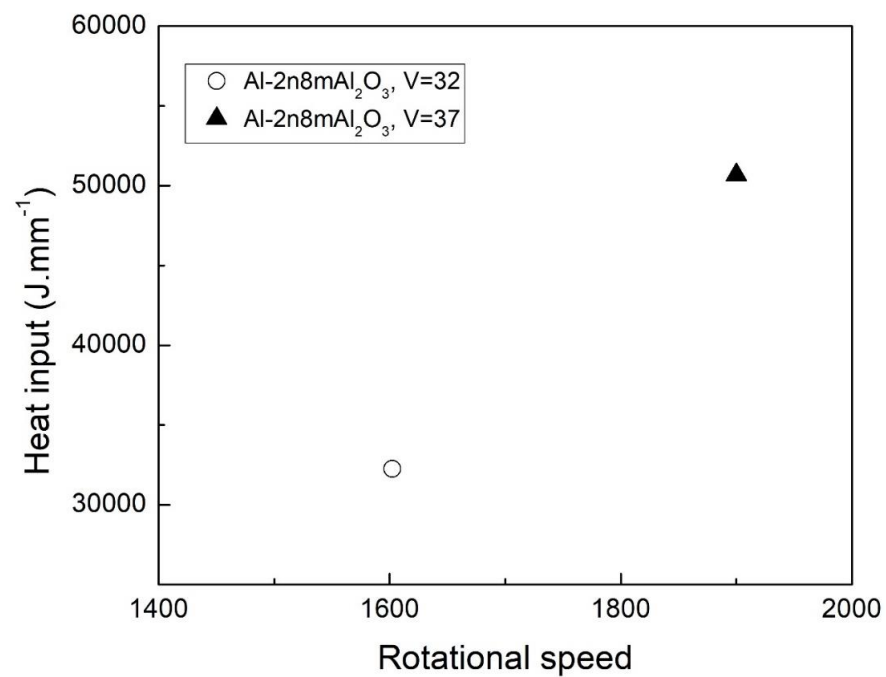
(**b**)

Figure 12. Force acting on the tool's main axis during friction stir welding performed at different processing parameters (**a**); corresponding heat input provided to the welding material (**b**).

At the start of the experiment, the temperature of the material is low. Its yield strength is high. Higher force values at the initial stage lead to tool penetration. The Fz is induced by the softening material when the tool penetration is complete, before the travel movement starts.

The microstructure of the nugget zone of the welds for the different employed processing parameters is shown in Figure 13. The particles are uniformly distributed, resembling nuggets. The presence of cracks is negligible. The presence of porosity and voids is greatly decreased in comparison with sintering.
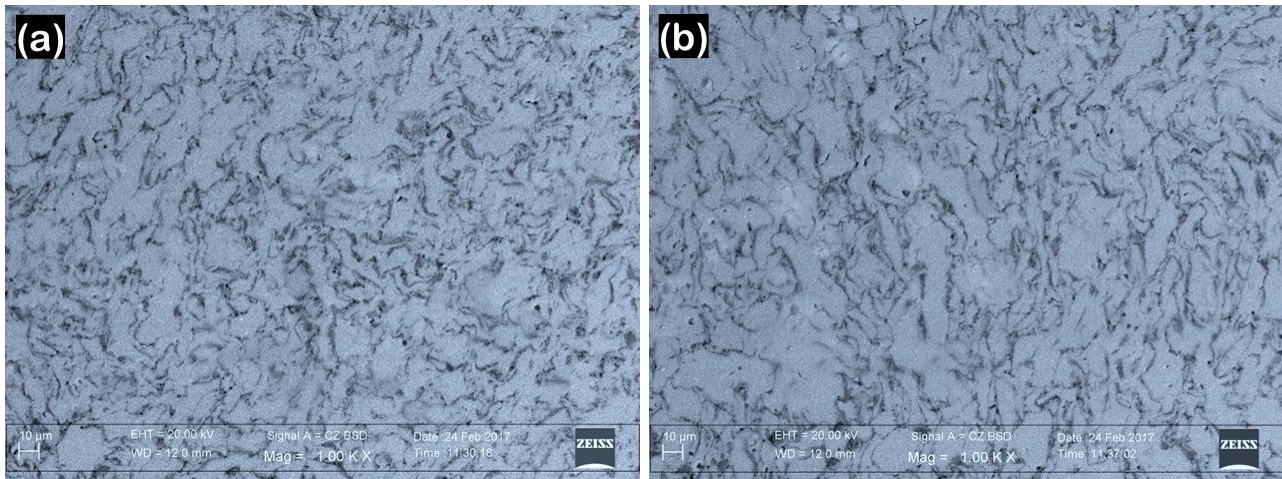

Figure 13. Nugget zone microstructure: 1600 RPM-32 mm/min (**a**), 1900 RPM-37 mm/min (**b**).

Intense plastic deformation during FSW, accompanied by the heat generated during the process, noticeably homogenized the overall preferential orientation of the Al grain structure and led to a new microstructure of Al grains compared to the SPSed microstructures. Indeed, the presence of nanosized particles, when agglomerated, and micron Al_2O_3 particles within weld zones during FSW processing can cause the stimulation of preferred nucleation sites via the particle-stimulated nucleation mechanism for the formation of new grains during dynamic recrystallization [28,48]. The average grain size of Al was 9 μm at 1900 RPM-37 mm/min, while it was around 6 μm at 1600 RPM-32 mm/min. Higher FSW processing parameters lead to higher heat input, which in turn diminishes the Zener pinning effect of Al_2O_3 nanoparticles. A similar finding was noted for the FSW of bimodal-reinforced Al-based composites [1,3,14]. In the heat-affected zone, the material experiences only a thermal effect on the grain behavior (grain growth), while in the nugget zone, the formation of cells and subgrain structures during dynamic recovery, and their conversion to new grains through continuous recrystallization in the nugget zone, have a significant role in the enhancement of the mechanical properties, especially hardness.

The microhardness profile for all the studied conditions is shown in Figure 14.

The microhardness profiles were described from measurements performed at the center of the weld cross-section. FSW of bimodal-reinforced Al-Al_2O_3 composites was accompanied by an increase in the hardness of the nugget zone, while softening was noticed for the base metal. It was reported that the heat input significantly affected the mechanical response of the welded materials [13,28]. Hardness increases upon increasing the heat input, which in turn contributes to the strong grain refinement during FSW, specifically in the nugget zone, due to the severe plastic deformation, and to the uniform distribution of reinforcing particles during processing [13,28]. The hardness values of SPSed samples were given in our previous papers, reaching approximately 60 HV [1]. Comparing the hardness values, it is revealed that the hardness of the nugget zone of FSWed samples in both conditions is higher than that of the SPEed sample with the same reinforcement content. In addition, a significant ~28% and ~33% decrease in the hardness occurred at the base metal/nugget zone interface at 1600 RPM-32 mm/min and at 1900 RPM-37 mm/min, respectively. The decrease was rather steep, which points to the existence of a very narrow heat- and thermo-mechanically affected zone between the base metal and nugget zones. However, there are minor fluctuations in the hardness data both at 1600 RPM-32 mm/min

and at 1900 RPM-37 mm/min in the base metal and the nugget zone. The highest values are experienced by those welds presenting a more recrystallized microstructure. The obtained hardness value for the nugget zone was similar to the value reported by [13,49].
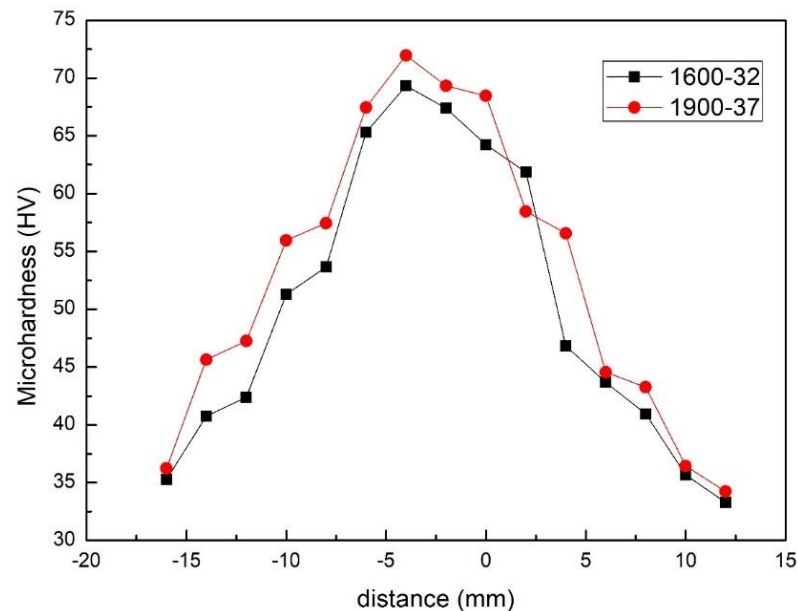
Figure 14. Microhardness profile for the different employed processing parameters.

The tensile curves for selected conditions are shown in Figure 15. It is reported that that heat input significantly affected the mechanical properties of the FSWed composites, especially bimodal-sized composites [28,50]. The strength of welded composite joints significantly varies with the rotational and traveling speeds, so the tensile strength increases when increasing the heat input. Comparing the tensile properties of the FSW joints indicates that the elongation of the welded joints in this study shows similar behavior to its tensile strength. In fact, at the same revolutionary pitch (rotational speed to traveling speed), the increase in the tool rotation leads to an increase in strength and ductility because of the different recrystallization behaviors of the stirred materials. Increasing the heat input (increasing ω and/or decreasing v) enhanced both the strength and elongation of FSWed joints. However, it is reported that at very high heat input, namely very high revolutionary pitch, a high temperature peak, accompanied by a slow cooling rate in the nugget zone, leads to the formation of coarse grains in the welded zone [13,28]. In turn, the presence of such a coarse grain region in the nugget zone results in a reduction in tensile strength. In brief, the optimum heat input, uniform distribution of nano- and micron-sized Al_2O_3 particles, high density and defect-free weld nugget region are the reasons for the enhancement in joint strength at an optimum heat input between 28,000 and 57,000 J/mm. Comparing the other aluminum-based composites with Al_2O_3 [13] and SiC [50], the tensile properties achieved in the current work could be obtained in a wide range of heat input. Indeed, the higher and wider range of heat input is attributed to the presence of the bimodal reinforcement of Al_2O_3 in the nugget zone, which is influenced by (1) the higher hardness, (2) the presence of closed or open pores and (3) the lower heat transfer coefficients of different elements in the nugget zone.
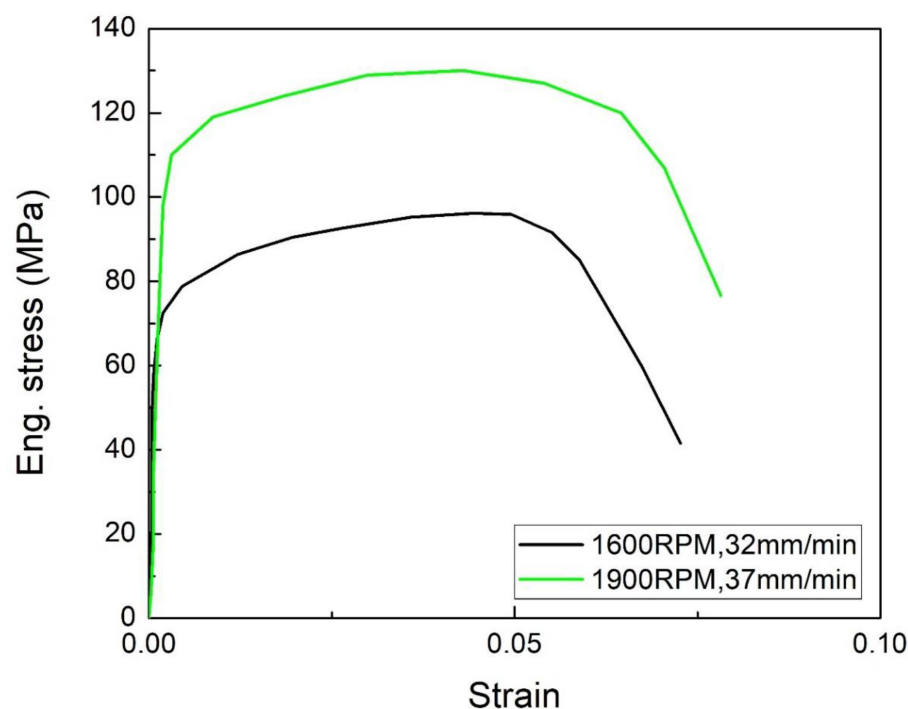
Figure 15. Tensile curves for selected friction stir welding conditions.

4. Conclusions

In the present paper, pure aluminum reinforced with nano-sized and micro-sized Al_2O_3 particles was produced via spark plasma sintering and friction stir welding. The material presents 3% porosity after sintering. All the material properties, including porosity, were employed to model the friction stir welding process in COMSOL MultiPhysics. The results show that upon increasing the tool rotating speed and the welding speed, the heat input and thermo-mechanical stresses increase in the material. This allows for improved material mixing (both matrix and reinforcement) and for a reduction in porosity. As a consequence, higher mechanical properties are revealed in the welded material. A sufficiently high heat input caused free flow, adequate plasticization and good consolidation of stirred metal at the weld nugget region. In turn, this causes a defect-free, fine-grained, uniform distribution of nano-sized and micro-sized Al_2O_3 particles, and a more hardened weld nugget region. These are the main reasons for the better tensile properties of the joints fabricated under this range of heat input.

Author Contributions: Conceptualization, B.S. (Behzad Sadeghi), B.S. (Behzad Sadeghian); Methodology, B.S. (Behzad Sadeghi), B.S. (Behzad Sadeghian); Software, B.S. (Behzad Sadeghi), A.G.; Validation, B.S. (Behzad Sadeghi), A.T., P.C.; Formal analysis, B.S. (Behzad Sadeghian), A.G., A.L.; Investigation, B.S. (Behzad Sadeghi), P.C.; Resources, B.S. (Behzad Sadeghi), A.T., P.C.; Data curation, P.C., B.S. (Behzad Sadeghian); Writing—original draft preparation, B.S. (Behzad Sadeghi), B.S. (Behzad Sadeghian); Writing—review and editing, B.S. (Behzad Sadeghi), P.C., A.L., A.G.; Visualization, B.S. (Behzad Sadeghi), P.C., A.T.; Supervision, P.C., A.T.; Project administration, B.S. (Behzad Sadeghi), P.C.; Funding acquisition, B.S. (Behzad Sadeghi). All authors have read and agreed to the published version of the manuscript.

Conflicts of Interest: The authors declare no conflict of interest.

References

1. Sadeghi, B.; Shamanian, M.; Ashrafizadeh, F.; Cavaliere, P.; Rizzo, A. Friction stir processing of spark plasma sintered aluminum matrix composites with bimodal micro- and nano-sized reinforcing Al_2O_3 particles. *J. Manuf. Process.* **2018**, *32*, 412–424. [CrossRef]
2. Cavaliere, P.; Sadeghi, B.; Shabani, A. Spark plasma sintering: Process fundamentals. In *Spark Plasma Sintering of Materials*; Springer: Berlin/Heidelberg, Germany, 2019; pp. 3–20.
3. Cavaliere, P.; Sadeghi, B.; Shamanian, M.; Ashrafizadeh, F. Al-Based Nanocomposites Produced via Spark Plasma Sintering: Effect of Processing Route and Reinforcing Phases. In *Spark Plasma Sintering of Materials: Advances in Processing and Applications*; Cavaliere, P., Ed.; Springer International Publishing: Cham, Switzerland, 2019; pp. 161–190.
4. Borrell, A.; Navarro, L.; Gutiérrez-González, C.F.; Alcázar, C.; Salvador, M.D.; Moreno, R. Microstructure and mechanical properties of 4YTZP-SiC composites obtained through colloidal processing and Spark Plasma Sintering. *Boletín De La Soc. Española De Cerámica Y Vidr.* **2021**, *60*, 175–182. [CrossRef]
5. Firestein, K.L.; Steinman, A.E.; Golovin, I.S.; Cifre, J.; Obraztsova, E.A.; Matveev, A.T.; Kovalskii, A.M.; Lebedev, O.I.; Shtansky, D.V.; Golberg, D. Fabrication, characterization, and mechanical properties of spark plasma sintered Al–BN nanoparticle composites. *Mater. Sci. Eng. A* **2015**, *642*, 104–112. [CrossRef]
6. Liu, Z.F.; Zhang, Z.H.; Lu, J.F.; Korznikov, A.V.; Korznikova, E.; Wang, F.C. Effect of sintering temperature on microstructures and mechanical properties of spark plasma sintered nanocrystalline aluminum. *Mater. Des.* **2014**, *64*, 625–630. [CrossRef]
7. Wolff, C.; Mercier, S.; Couque, H.; Molinari, A. Modeling of conventional hot compaction and Spark Plasma Sintering based on modified micromechanical models of porous materials. *Mech. Mater.* **2012**, *49*, 72–91. [CrossRef]
8. Babu, N.K.; Kallip, K.; Leparoux, M.; AlOgab, K.A.; Maeder, X.; Dasilva, Y.A.R. Influence of microstructure and strengthening mechanism of AlMg5–Al_2O_3 nanocomposites prepared via spark plasma sintering. *Mater. Des.* **2016**, *95*, 534–544. [CrossRef]
9. Izadi, H.; Nolting, A.; Munro, C.; Bishop, D.; Plucknett, K.; Gerlich, A. Friction stir processing of Al/SiC composites fabricated by powder metallurgy. *J. Mater. Process. Technol.* **2013**, *213*, 1900–1907. [CrossRef]
10. Guo, J.; Liu, J.; Sun, C.; Maleksaeedi, S.; Bi, G.; Tan, M.; Wei, J. Effects of nano-Al_2O_3 particle addition on grain structure evolution and mechanical behaviour of friction-stir-processed Al. *Mater. Sci. Eng. A* **2014**, *602*, 143–149. [CrossRef]
11. Cavaliere, P.; Jahantigh, F.; Shabani, A.; Sadeghi, B. Influence of SiO_2 nanoparticles on the microstructure and mechanical properties of Al matrix nanocomposites fabricated by spark plasma sintering. *Compos. Part B Eng.* **2018**, *146*, 60–68. [CrossRef]
12. Zhang, Q.; Xiao, B.; Wang, Q.; Ma, Z. In situ Al_3Ti and Al_2O_3 nanoparticles reinforced Al composites produced by friction stir processing in an Al-TiO_2 system. *Mater. Lett.* **2011**, *65*, 2070–2072. [CrossRef]
13. Khodabakhshi, F.; Ghasemi Yazdabadi, H.; Kokabi, A.H.; Simchi, A. Friction stir welding of a P/M Al–Al_2O_3 nanocomposite: Microstructure and mechanical properties. *Mater. Sci. Eng. A* **2013**, *585*, 222–232. [CrossRef]
14. Sadeghi, B.; Shamanian, M.; Cavaliere, P.; Ashrafizadeh, F.; Sanayei, M.; Szpunar, J.A. Microstructural and mechanical behavior of bimodal reinforced Al-based composites produced by spark plasma sintering and FSP. *Int. J. Adv. Manuf. Technol.* **2018**, *94*, 3903–3916. [CrossRef]
15. Zangabad, P.S.; Khodabakhshi, F.; Simchi, A.; Kokabi, A. Fatigue fracture of friction-stir processed Al–Al_3Ti–MgO hybrid nanocomposites. *Int. J. Fatigue* **2016**, *87*, 266–278. [CrossRef]
16. Deng, D. FEM prediction of welding residual stress and distortion in carbon steel considering phase transformation effects. *Mater. Des.* **2009**, *30*, 359–366. [CrossRef]
17. Darvazi, A.R.; Iranmanesh, M. Prediction of asymmetric transient temperature and longitudinal residual stress in friction stir welding of 304L stainless steel. *Mater. Des.* **2014**, *55*, 812–820. [CrossRef]
18. Riahi, M.; Nazari, H. Analysis of transient temperature and residual thermal stresses in friction stir welding of aluminum alloy 6061-T6 via numerical simulation. *Int. J. Adv. Manuf. Technol.* **2011**, *55*, 143–152. [CrossRef]
19. Khandkar, M.Z.H.; Khan, J.A.; Reynolds, A.P.; Sutton, M.A. Predicting residual thermal stresses in friction stir welded metals. *J. Mater. Process. Technol.* **2006**, *174*, 195–203. [CrossRef]
20. El-Sayed, M.; Shash, A.; Abd-Rabou, M. Finite element modeling of aluminum alloy AA5083-O friction stir welding process. *J. Mater. Process. Technol.* **2018**, *252*, 13–24. [CrossRef]
21. Kaviany, M. *Principles of Heat Transfer in Porous Media*; Springer Science & Business Media: Berlin/Heidelberg, Germany, 2012.
22. Bejan, A. *Convection Heat Transfer*; John Wiley & Sons: Hoboken, NJ, USA, 2013.
23. Sadeghian, B.; Taherizadeh, A.; Atapour, M. Simulation of weld morphology during friction stir welding of aluminum-stainless steel joint. *J. Mater. Process. Technol.* **2018**, *259*, 96–108. [CrossRef]
24. Schmidt, H.B.; Hattel, J.H. Thermal and material flow modelling of friction stir welding using Comsol. In Proceedings of the Proceedings of the COMSOL Conference 2008, Hannover, Germany, 5 November 2008.
25. Schmidt, H.; Hattel, J. A local model for the thermomechanical conditions in friction stir welding. *Model. Simul. Mater. Sci. Eng.* **2004**, *13*, 77. [CrossRef]
26. Nandan, R.; Roy, G.; Lienert, T.; DebRoy, T. Numerical modelling of 3D plastic flow and heat transfer during friction stir welding of stainless steel. *Sci. Technol. Weld. Join.* **2006**, *11*, 526–537. [CrossRef]
27. Nandan, R.; Roy, G.; Lienert, T.; Debroy, T. Three-dimensional heat and material flow during friction stir welding of mild steel. *Acta Mater.* **2007**, *55*, 883–895. [CrossRef]
28. Sadeghi, B.; Shamanian, M.; Ashrafizadeh, F.; Cavaliere, P. FSW of bimodal reinforced Al-based composites produced via spark plasma sintering. *Int. J. Mater. Res.* **2017**, *108*, 1045–1054. [CrossRef]

29. Garbiec, D.; Jurczyk, M.; Levintant-Zayonts, N.; Mościcki, T. Properties of Al–Al$_2$O$_3$ composites synthesized by spark plasma sintering method. *Arch. Civ. Mech. Eng.* **2015**, *15*, 933–939. [CrossRef]

30. Eldesouky, A.; Johnsson, M.; Svengren, H.; Attallah, M.; Salem, H. Effect of grain size reduction of AA2124 aluminum alloy powder compacted by spark plasma sintering. *J. Alloy. Compd.* **2014**, *609*, 215–221. [CrossRef]

31. Rahimian, M.; Parvin, N.; Ehsani, N. Investigation of particle size and amount of alumina on microstructure and mechanical properties of Al matrix composite made by powder metallurgy. *Mater. Sci. Eng. A* **2010**, *527*, 1031–1038. [CrossRef]

32. Sadeghi, B.; Shamanian, M.; Ashrafizadeh, F.; Cavaliere, P.; Sanayei, M.; Szpunar, J.A. Microstructural behaviour of spark plasma sintered composites containing bimodal micro- and nano-sized Al$_2$O$_3$ particles. *Powder Metall.* **2018**, *61*, 50–63. [CrossRef]

33. Sadeghi, B.; Shamanian, M.; Ashrafizadeh, F.; Cavaliere, P. Effect of processing parameters on microstructural and mechanical properties of aluminum–SiO$_2$ nanocomposites produced by spark plasma sintering. *Int. J. Mater. Res.* **2018**, *109*, 422–430. [CrossRef]

34. Sadeghi, B.; Shabani, A.; Cavaliere, P. Hot rolling of spark-plasma-sintered pure aluminium. *Powder Metall.* **2018**, *61*, 285–292. [CrossRef]

35. Sadeghi, B.; Cavaliere, P.; Balog, M.; Pruncu, C.I.; Shabani, A. Microstructure dependent dislocation density evolution in micro-macro rolled Al$_2$O$_3$/Al laminated composite. *Mater. Sci. Eng. A* **2022**, *830*, 142317. [CrossRef]

36. Sadeghi, B.; Cavaliere, P.; Pruncu, C.I.; Balog, M.; Marques de Castro, M.; Chahal, R. Architectural design of advanced aluminum matrix composites: A review of recent developments. *Crit. Rev. Solid State Mater. Sci.* **2022**, 1–71. [CrossRef]

37. Dash, K.; Chaira, D.; Ray, B.C. Synthesis and characterization of aluminium–alumina micro-and nano-composites by spark plasma sintering. *Mater. Res. Bull.* **2013**, *48*, 2535–2542. [CrossRef]

38. Sadeghi, B.; Cavaliere, P.; Nosko, M.; TremboŠová, V.; Nagy, Š. Hot deformation behaviour of bimodal sized Al$_2$O$_3$/Al nanocomposites fabricated by spark plasma sintering. *J. Microsc.* **2021**, *281*, 28–45. [CrossRef]

39. Sadeghi, B.; Shamanian, M.; Ashrafizadeh, F.; Cavaliere, P.; Rizzo, A. Wear Behavior of Al-Based Nanocomposites Reinforced with Bimodal Micro- and Nano-Sized Al$_2$O$_3$ Particles Produced by Spark Plasma Sintering. *Mater. Perform. Charact.* **2018**, *7*, 20180039. [CrossRef]

40. Zhu, X.; Chao, Y. Numerical simulation of transient temperature and residual stresses in friction stir welding of 304L stainless steel. *J. Mater. Process. Technol.* **2004**, *146*, 263–272. [CrossRef]

41. Sadeghian, B.; Taherizadeh, A.; Atapour, M.; Saeidi, N.; Alhaji, A. Phase-field simulation of microstructure evolution during friction stir welding of 304 stainless steel. *Mech. Mater.* **2021**, *163*, 104076. [CrossRef]

42. Zhang, J.; Shen, Y.; Li, B.; Xu, H.; Yao, X.; Kuang, B.; Gao, J. Numerical simulation and experimental investigation on friction stir welding of 6061-T6 aluminum alloy. *Mater. Des.* **2014**, *60*, 94–101. [CrossRef]

43. Poolperm, P.; Nakkiew, W.; Naksuk, N. Finite element analysis of the effect of porosity on residual stress in 2024 aluminium alloy GTAW. *Mater. Res. Express* **2020**, *7*, 056518. [CrossRef]

44. Poolperm, P.; Nakkiew, W. Effect of porosity on residual stress of 2024-aluminum GTAW specimen. *Mater. Sci. Forum* **2016**, *872*, 28–32. [CrossRef]

45. Cavaliere, P.; Campanile, G.; Panella, F.; Squillace, A. Effect of welding parameters on mechanical and microstructural properties of AA6056 joints produced by Friction Stir Welding. *J. Mater. Process. Technol.* **2006**, *180*, 263–270. [CrossRef]

46. Cavaliere, P.; De Santis, A.; Panella, F.; Squillace, A. Effect of welding parameters on mechanical and microstructural properties of dissimilar AA6082–AA2024 joints produced by friction stir welding. *Mater. Des.* **2009**, *30*, 609–616. [CrossRef]

47. Cavaliere, P.; Cabibbo, M.; Panella, F.; Squillace, A. 2198 Al–Li plates joined by friction stir welding: Mechanical and microstructural behavior. *Mater. Des.* **2009**, *30*, 3622–3631. [CrossRef]

48. Bodaghi, M.; Dehghani, K. Friction stir welding of AA5052: The effects of SiC nano-particles addition. *Int. J. Adv. Manuf. Technol.* **2017**, *88*, 2651–2660. [CrossRef]

49. Balog, M.; Orovcik, L.; Nagy, S.; Krizik, P.; Nosko, M.; Oslanec, P.; Zifcak, P. To what extent does friction-stir welding deteriorate the properties of powder metallurgy Al? *J. Mater. Res. Technol.* **2020**, *9*, 6733–6744. [CrossRef]

50. Periyasamy, P.; Mohan, B.; Balasubramanian, V. Effect of heat input on mechanical and metallurgical properties of friction stir welded AA6061-10% SiCp MMCs. *J. Mater. Eng. Perform.* **2012**, *21*, 2417–2428. [CrossRef]